Design and Synthesis of a Micro-Glider

gliderobot.weebly.com

Alvaro Azabal, Ayanle Aden, Jacob Benoliel, Manuel Arbelo, Mansoor Aman, Mohammad Beit-Sadi, Wey Han

***Abstract*— Gliding is an efficient and versatile way to traverse large distances whilst expending as little energy as possible. Work done in the field of biomimetic robotics has demonstrated further benefits to gliding in increasing trajectory control and reducing landing impact loads. A small-scale micro-glider was built to fit a specific design envelope with the objective of maximizing its glide range. A linear dynamics model was used to design and predict the gliding performance of the robot. Once manufactured, it achieved a glide distance of 1.8m and the performance was accurately captured by the dynamics model.**

I. Introduction

Energy efficient locomotion is one of the major challenges in small scale mobile robotics. Gliding is used by various animals such as spiders, bats and lizards, to overcome obstacles and rough terrain. It prolongs powered flight, extends horizontal range and reduces landing impact loads.

A micro-glider was designed to fit the following specifications:

- Constant mass of less than 50g
- Maximum dimension of 40 cm
- Single remote controlled motor used for actuation
- No active propulsion during glide phase

The objective of the design was to achieve the maximum horizontal distance, as shown in Figure 1.

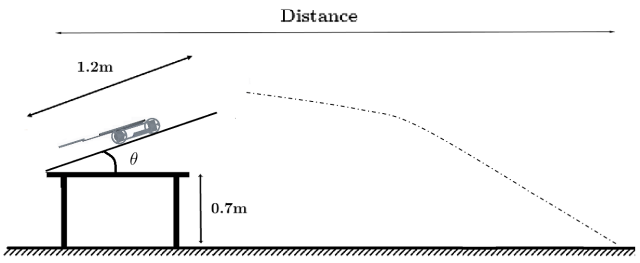

Fig. 1. Diagram of mission profile

II. Terrestrial Model

The objective of the terrestrial modelling was to maximize the end of ramp velocity, such that a stable glide occurs swiftly after take-off. The modelling was done using the kinematic equations of motion and rotational dynamics:

$$\mu N_r - mgsin(\theta) - D = m\ddot{x} \tag{1}$$

$$\tau - I\dot{\alpha} = \mu N_r r \tag{2}$$

The drag (D) in Equation 1 was simplified to the drag on a spherical bluff body of a similar characteristic length, this assumption is justified by the low Reynolds numbers. The motor torque is a function of the angular velocity the shaft ($\tau = f(\dot{\alpha}$. The normal reaction (N_r) at the wheels and the inertia of the drivetrain (I) were determined by a preliminary CAD model. The coefficient of friction (μ) between the wheels and the ramp surface was determined experimentally. These equations can be restated in terms of the angular velocity ($\dot{\alpha}$):

$$\ddot{\alpha} + \kappa_1\dot{\alpha}^2 + \kappa_2\alpha = \kappa_3 \tag{3}$$

$$\kappa_1 = \frac{\rho r^3 SC_d}{I + r^2 m},\ \kappa_2 = \frac{\tau_{stall}/\omega_{stall}}{I + r^2 m},\ \kappa_3 = \frac{\tau_{stall} - mgrsin(\theta)}{I + r^2 m}$$

This was solved numerically for a range of ramp angles to determine the end of ramp speed.

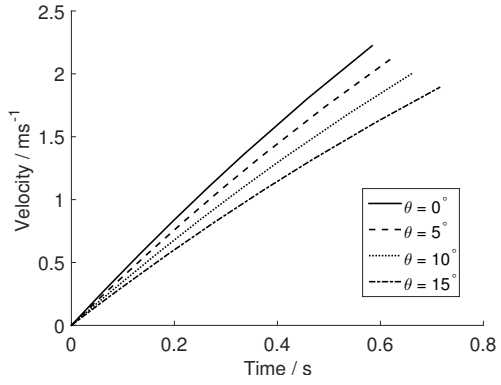

Fig. 2. Linear velocity against time for a range of ramp angles

The optimal ramp angle to achieve maximum end of ramp velocity is between $0° - 5°$. To prevent wheel slip due to loss of traction, the motor torque ramping profile has to be consistent with:

$$\tau_{max} \leq \left(\frac{I}{mr} + r\right)\mu N_r - \frac{Ig}{r} sin(\theta) \tag{4}$$

III. Glide Model

A transition phase occurs between the ramp take-off and glide phase. The robot goes into an accelerated descent until it reaches its glide velocity and trim angle. For simplicity, it was assumed that the transition phase ends when the glider reaches the same height as the ends of the ramp. The glide model includes only the longitudinal dynamics, it is assumed that the glider will be laterally symmetric. If proven otherwise by testing, a vertical tail can be added to restore lateral stability. The dynamics can be presented in state space form:

$$\mathbf{M}(\ddot{\mathbf{x}}) = \mathbf{N}(\mathbf{x}) + \mathbf{F}(\mathbf{x}, \dot{\mathbf{x}}) + \mathbf{G}(\mathbf{x}) \tag{5}$$

These are derived from Newton's second law and Euler's equation transformed to a body centred reference frame; they apply only to rigid wing aircraft. For simplicity, the non-linearity matrix (**N**) is ignored. The assumptions made for the aerodynamics forces (**F**) are that the lift is generated entirely by the wings and the drag will be approximated as described in the terrestrial modelling. In steady glide, the pitch angle is assumed to vary smoothly with velocity.

$$\frac{d}{dt}\begin{bmatrix}\theta \\ v\end{bmatrix} = \begin{bmatrix}\frac{\frac{1}{2}\rho S}{m} C_L v - \frac{g cos\theta}{v} \\ -g sin\theta - \frac{\frac{1}{2}\rho S}{m} C_D v^2\end{bmatrix} \tag{6}$$

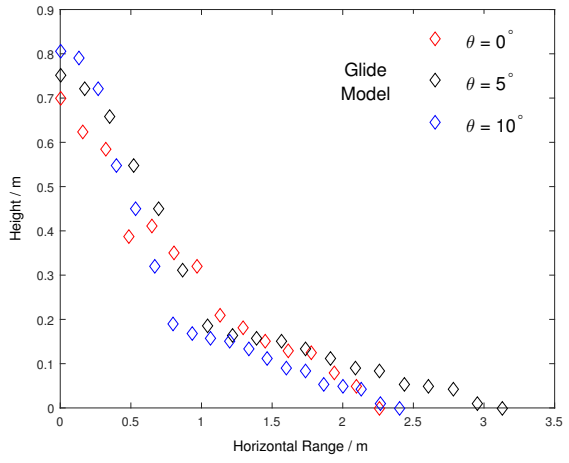

Fig. 3. Glide trajectory predicted by the numerical model

The model predicts a horizontal range of 2.4 - 3.2 m, for a ramp angle 0°- 5° and take-off speed of $2ms^{-1}$.

IV. Structural Consideration

The glider must perform several consecutive test runs, so it is important to verify that the landing impact does not cause any significant damage. The glide phase can end in stall and this may result a nose down landing. The impact is substantially less than in the case of a pure jump with no glide, so the body was designed to fail at this landing impact stress (Figure 4). The wheels are manufactured from foam to absorb some of the impact energy. The mass of the glider, predicted by the CAD model was 42 g.

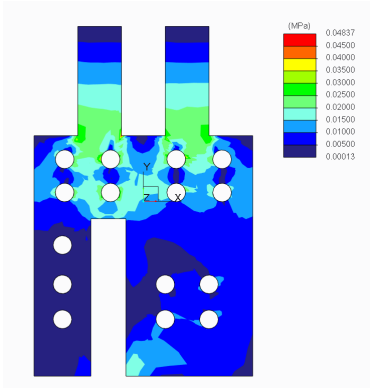

Fig. 4. Dynamic FEA analysis of peak landing impact stress

V. Manufacturing

A. Glider body

The material choices were constrained by weight limitations. The chassis was laser cut from thin sheets of acetal. This material provided sufficient stiffness during operation and is tough enough to withstand the deformations during landing. The electric motor was linked by 1:1 spur gears to the rear axle, with a passively driven front wheel. The micro-controller and battery were placed on the base plate (Figure 4) such that the centre of mass lies at the lateral centre of the base plate. All components were glued with epoxy.

B. Wing and Tail

The wing was laser cut from 3mm Depron foam, a lightweight material with high specific stiffness. To achieve a cambered flat plate, the wing was heated and pressed onto a cylindrical template. The surface was sanded to a smooth finish. A non-cambered flat plate was used for the tail and the tail booms were constructed from carbon fibre rods. The actual mass of the glider was 49.7 g.

VI. Performance

The glider had 5 consecutive test runs off a ramp at a height of 0.7 m above ground. The horizontal glide distance was measured as the position of rear-most point of the glider, at the moment of impact. The ramp angle was varied between 0°-5°. The approximate speed, as measured from the high speed video recording indicated a take-off velocity of 0.8 ms^{-1}. The foam wings showed noticeable deflection during glide. The horizontal displacement from the end of the ramp was 1.8 m, giving an average glide ratio of 1.4 (taking into account the transition phase). The performance without the wings resulted in an end of ramp speed of 1.4 ms^{-1} but a horizontal range of only 1.5m.

VII. Discussion

A. Ramp climb

Initial testing showed that the motor torque ramping profile had to be modified as a step profile to maximum power resulted in loss of traction. The friction in the drivetrain was not negligible. These factors, coupled with the underestimated mass resulted in a significantly lower end of ramp speed than the predicted $2ms^{-1}$. The manufacturing of the terrestrial component of the glider was sufficiently accurate with no misalignment of components.

B. Glide

The low aspect ratio cambered flat plate offered a significant improvement over conventional high aspect ratio swept wings. The low aspect ratio was required for sufficient lifting area and the larger chord length was less conducive to separation. The trimmed glide angle was small so camber was required to provide sufficient lift at low angles of attack.

The actual performance was slightly less than the predicted range (Figure 5), although these discrepancies are well understood. The lower ramp take-off speed resulted in a long transition phase, as the glider had to accelerate for a longer period (under the action of gravity) before attaining glide velocity. Due to manufacturing imprecision, the wing was mounted with a slight bank angle, giving the glider a tendency to turn right during flight. The actual distance travelled was further than the horizontal displacement measured. The focus of mass towards the longitudinal axis of symmetry reduced the lateral inertia ($I_{\bar{Z}\bar{Z}}$) of the glider, making it susceptible to even the slightest perturbations. Finally the drag of the wing was not

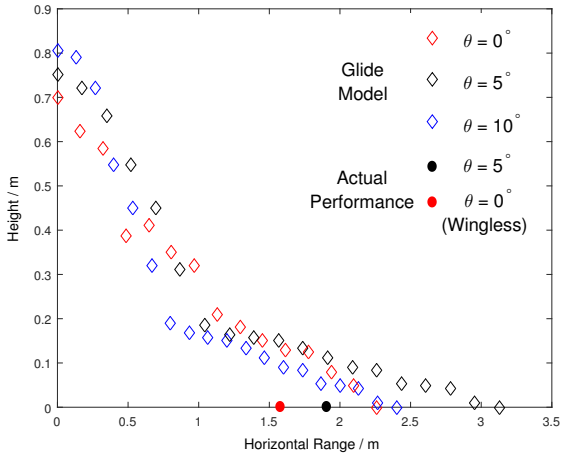

Fig. 5. Comparison of model to experimental results

negligible as assumed in the glide model because of the low aspect ratio. However the wings did improved horizontal range; the wingless robot only reached 1.55 m and shattered on impact.

The longitudinal glide dynamics model was reasonably accurate in its predictions. The horizontal range, glide velocity and pitch angle were all accurate within margin of error and manufacturing tolerances. With the potential of high precision additive manufacturing, these uncertainties can be minimized and by extension the discrepancies between the modelled dynamics and actual performance.

VIII. Conclusion

The experimental results are in agreement with the predictions of the linear glide dynamics model. The glider achieved a horizontal range of 1.8m (75% of predicted range), out performing the wingless robot and reducing landing impact loads. Improvements could be made to reduce the weight of the design, which would substantially increase the range of the glider, both by increasing the end of ramp speed and reducing the required lift (size of the wing). Other ideas include deployable wings that fold during the ramp climb phase and deploy once the glider is airborne.

References

[1] A. Vidyasagar, J.-C. Zufferey, D. Floreano, and M. Kovac, "Performance analysis of jump-gliding locomotion for miniature robotics," *Bioinspiration & Biomimetics*, vol. 10, no. 2, p. 025006, 2015.

[2] A. L. Desbiens, P. M, F. Berg, Z. E. Teoh, J. Lee, and M. Cutkosky, "Efficient jumpgliding: Theory and design considerations," *IEEE*, 2013.